First principles study: Structure, stability and thermodynamics of intrinsic point defects in indium oxide

Péter Ágoston[1], Paul Erhart[2], Andreas Klein[1], and Karsten Albe[1]
[1]*Institut für Materialwissenschaft, Technische Universität Darmstadt, Petersenstr. 23, D-64287 Darmstadt, Germany and*
[2]*Lawrence Livermore National Laboratory*
(Dated: November 29, 2007)

We have conducted an extensive study on intrinsic point defects in In_2O_3 by means of first principles calculations within density functional theory. Defect geometries of vacancies, interstitials and anti-sites are investigated, and their electronic structure is discusssed in detail. The calculations were performed using the GGA+U approximation which leads to an improved description of electronic structures and geometries. Finite size effects were corrected by an extrapolation procedure in order to obtain defect formation energies for infinite dilution. Oxygen vacancies were found to be shallow donor defects explaining the *n*-type conductivity as well as non-stoichiometry in In_2O_3. Further, we show that oxygen interstitials exist in different dumbbell geometries forming covalently bonded structures at higher oxygen partial pressures.

PACS numbers: 61.72.Bb, 61.72.Ji, 61.82.Fk

I. INTRODUCTION

Indium oxide (In_2O_3) is a *Transparent Conducting Oxide* (TCO), similar to SnO_2 and ZnO . They exhibit good conductivity while lacking optical excitations within the visual range[1,2]. In optoelectronics, and especially for applications involving organic materials such as (OLEDs)[3] and (OPVs)[4,5] tin-doped In_2O_3 (Indium Tin Oxide) is the primary choice[6]. For this material free electron-like conductivity is found[7] with carrier concentrations of about $10^{21}\ \mathrm{cm}^{-3}$. Further, In_2O_3 also exhibits good gas sensing properties especially for oxygen and ozon[8]. Remarkably, even the undoped material is *n*-type conducting[9] with carrier concentrations of up to $10^{19}\ \mathrm{cm}^{-3}$. This intrinsic conductivity is accounted to intrinsic donor point defects due to the pronounced non-stoichiometry found in the structure at highly reducing conditions. From the experimental point of view, both the non-stoichiometry and the *n*-type conductivity have been believed to originate from doubly charged oxygen vacancies[9]. Oxygen realted defects play a major role in gas sensors[8], and may also cause fatigue in applications with organic materials[10].

Due to the experimental findings the oxygen vancancy in In_2O_3 was firstly studied using density functional thory (DFT) within the generalized gradient approximation (GGA) beside several other oxide materials[11,12]. Although calculations were performed in three charge states no finite size effects were considered. Tomita *et al.* conducted molecular orbital cluster calculations and also mainly focused on donor defect types including defect complexes of oxygen vacancies and indium interstitials[13]. In contrary to Tanaka *et al.*[11,12] indium interstitial defects and defect complexes consisting of indium interstitial and oxygen vacancies were found to produce shallow donor transition energies. However, only the electronic properties of unrelaxed defective clusters were investigated within the study. Neither formation energies, nor different charge states were considered. Recently, a defect model was presented by Lany *et al.*[14]. Within this study it is concluded that no intrinsic point defect is capable of producing electron densities found in reduced samples. Since some indication for a localized character of the oxygen defect states was found, it was concluded that counductivity should originate from a photo induced process. According to Lany *et al.* the oxygen vacancy is a neutral color center with well localized electrons on the defect. By subsequently absorbing two photons and an energy barrier due to relaxation processes inhibiting the decay, a persistent conductivity should be obtained also explaining the coloring. To our knowledge no direct evidence for such a mechanism was found in In_2O_3. In contrast to ZnO the defect chemistry of In_2O_3 has not been extensively studied from the theoretical point of view.

Within this study we conduct extensive defect calculation using plane wave pseudopotential formalism of DFT. We attempt to obtain a more complete and consistent picture about the intrinsic defect chemistry of In_2O_3. We perform defect calculations using the GGA+*U* for exchange correlation in order to achieve a better description of the electronic structure and defect relaxation. We include antisites as well as various dumbell and split interstitial oxygen defect geometries as they were not yet discussed. In previous studies on ZnO, a related material, we showed that the wurzite structure can accomodate various covalently bonded oxygen interstitial geometries[15]. Finally, we discuss changes in the electronic structure induced by the defects in order to evaluate the applicability of band gap corrections. We show that all intrinsic donor defects do have shallow states and are capapable of producing free electrons in the conduction band and identify the oxygen vacancy as the major donor due to low formation energy. For oxidized material we show that there is wealth of dumbbell like defect geometries for oxygen.

II. METHODOLOGY

A. Computational setup

For defect calculations, as presented in the following sections, the plane-wave pseudo-potential (PW-PP) implementation of the Vienna ab-initio Simulation Package (Vasp)[16,17] was used. For representation of the ionic cores, the projector augmented wave (PAW) scheme by Blöchl[18,19] was employed.

For Brillouin-zone integration, a Γ-centered $3 \times 3 \times 3$ *k*-point mesh was used with a varying number of *k*-points within the irreducible Brillouin zone depending on symmetry for different defects. During defect calculations, the volume of the supercell was kept constant at the calculated value of the ideal cell. With this constraint the ionic relaxation was stopped when forces on ions were converged to less than 10 meV/Å. Indium 4*d*, 5*s*, 5*p*, and oxygen 2*s*, 2*p* electrons were treated as part of the valence. For exchange-correlation functional, the GGA parameterized by Perdew, Burke and Ernzerhof (PBE)[20] was used with a self-interaction correction scheme (GGA+U) described in the following paragraph. The cut-off energy of the wave function plane wave expansion was set to 500 eV. Using this setup the calculated properties for In_2O_3 agree well with experimental values (TableI).

1. *Finite cell-size corrections*

The defect calculations were carried out using four different cell sizes in order to asses the effect of finite system size. Two were based on the body centered cubic unit cell with 80 atoms ($1 \times 1 \times 1$ and $2 \times 2 \times 2$) and another two were created using the primitive rhombohedral 40 atom unit cell of the bixbiyte structure ($1 \times 1 \times 1$ and $3 \times 1 \times 1$). Due to periodic boundary conditions, unphysical interactions between a defects with its images are introduced at high concentrations. Therefore an extrapolation precedere was used for the defect formation energies[21] in order to obtain formation energies at infinite dilution. Before extrapolating the formation energies versus the inverse cell volume, we substracted the binding Madelungen energy of a point charge with the compensating jellium background charge[22] . For this purpose we used the static dielectric constant of $\epsilon = 8.9$ determined by optical measurements[1].

2. *Charge and barrier analysis*

In order to see how charge is redistributed during defect formation, and to what extent it is localized on defects we use the Bader charge analysis[23] in order to otain the integrated electron density within a region around the ion in question delimited by the minima within charge density.

As we find different oxygen interstitial configurations with thermally accesible formation energies, we use the climbing image nudge elastic band method[24–26] (CI-NEB), in order to find the transition energies. Several intermediate images are relaxed with spring forces acting inbetween so that the images do not see a force along the band tangent This way, the images converge into the low energy path.

3. *GGA+U method*

DFT calculations on semiconductors are severely hampered by the DFT band gap problem[27,28]. For In_2O_3 the case is even more problematic since the actual band gap is not known as we discussed before[29] (and references therein). Optical measurements indicated indirect transitions (~ 2.6 eV) beside the direct (~ 3.6 eV)[30] and further, XPS/UPS meassurements[31,32] yield systematically too low Fermi energies also indicating either surface states or an indirect or optically forbidden band gap. Since the band gap marks the energy scale for transition levels, and also can affect formation energies, an uncertainty of up to 1eV may change the picture also qualitatively. The transition levels which indicate the electronic properties of point defects critically depend on the choice of the band gap error correction[33], beside finite size corretions. As the GGA band gap is about 0.93eV[29] compared with experimental values ranging from 2.62-3.75eV[30], the introduced error is exeptionally high for this material and also affected previous defect studies on In_2O_3[11,12,14]. In this context defect calculations with a better discription of the electronic structure would be desirible. Since spurious self-interactions are partly responsible for the discrepancies between calculated and experimental band structure[34,35], the GGA+U method[36,37] was used within the present work to remedy some of this error. Within Dudarev's approach[38], there is only one free orbital dependent parameter, $\bar{U} - \bar{J}$, which can be varied. $\bar{U}$ and $\bar{J}$ are the spherically averaged matrix elements of the screened Coulomb electron-electron interaction. Although,it is well known that DFT underestimates band gaps, the error is exceptionally high for $In_2O_3$with GGA only. Further, the indium 4*d* semi-core bands are too close to the VBM as compared to experimental photoelectron spectroscopy data.[34,35] The effect of unphysical self-interaction is large at high electron densities and localized states so that for In_2O_3, the indium 4*d* semicore band, is strongly affected by it, resulting in underbinding. Using band structure calculations[29] it was shown that for $\bar{U} - \bar{J} = 7$, the electronic density of states (DOS) agrees very well with experimental data[34,35]. We perform all defect calculations as well as calculations on the ideal cell with this correction, whereas it was not applied for metallic indium, which would be unphysical. The GGA+U method can also applied *a posteriori* by correcting the VB edge by the GGA+U value as it was done by Lany[14] for In_2O_3. However, since both band edges shift upwards with increasing $\bar{U} - \bar{J}$ parameter we find it problematic to apply a downward shift to the VBM. Further, we have shown[29], that also the description of structural parameters is improved by the GGA+U method, which results in a better description of ionic relaxation in defect calculations.

B. Formation energies

The Gibbs free energy for the creation of a charged point defect in the two component system In_2O_3 can be expressed as

$$\begin{aligned} \Delta G_D(E_f, \mu) &= G_{Def} - G_0 \\ &- \Delta n_{\mathrm{In}}(\mu_{\mathrm{In}}^{\mathrm{In}} + \Delta\mu_{\mathrm{In}}) \\ &- \Delta n_{\mathrm{O}}(\mu_{\mathrm{O}}^{\mathrm{O}_2} + \Delta\mu_{\mathrm{O}}) \\ &+ q(E_{VBM} + E_f), \end{aligned} \tag{1}$$

TABLE I: Experimental data for bixbiyte-In_2O_3, elemental indium and oxygen compared with calculated properties using GGA-PBE. Agreement with experiment is improved using GGA+*U*, except for the formation energies of the compound semiconductor. E_c: is thecohesive energy (eV/f.u.), a_0 lattice constant (Å), V_0 cell volume (Å^3), E_G band gap (eV), H^f formation energy of compound (eV/f.u) and D_0 dimer dissociation energy (eV)

		Exp.	GGA-PBE $\bar{U}-\bar{J}=0$	GGA-PBE $\bar{U}-\bar{J}=7$
In_2O_3	E_c		28.27	29.29
	a_0	10.121[39]	10.306	10.027
	V_0	64.80[39]	68.41	63.01
	E_G	2.5-3.75[30]	0.93	1.79
	H^f	9.596[40]	9.61	10.63
Indium	E_c		-2.728	
	a_0	3.332[40]	3.281	
	c/a	1.342[40]	1.479	
	V_0	49.644[40]	52.238	
Oxygen	D_e	5.17[40]	4.4	
	a_0	1.208[40]	1.23	

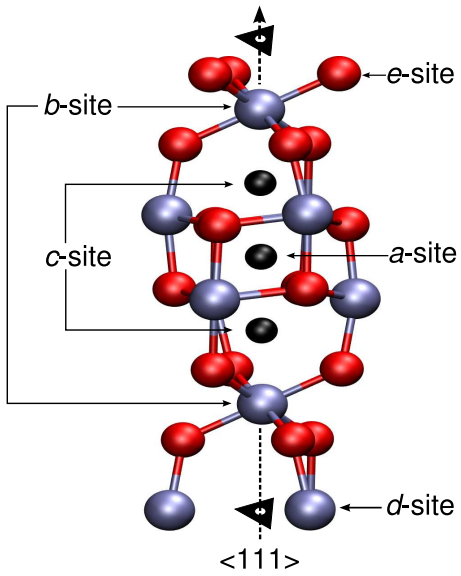

FIG. 1: Arrangement of atoms surrounding the $\langle 111\rangle$ threefold axis. Black spheres denote interstitial sites enclosed by two regular indium *b*-sites in the order *b*-*c*-*a*-*c*-*b*. Indium atoms are also located on *d*-sites which have a two-fold point symmetry. Oxygen atoms reside on the general *e*-site

where G_0 and G_{Def} are the total free energies of the ideal and the defective supercell, respectively. The Δn_i count the number of exchanged atoms of the species i, $\Delta\mu_i$ denote the deviation of the chemical potentials in the compound from that of the elemental phases μ_i. The chemical potential of the electrons is the Fermi energy E_f which is typically meassured from the valence band maximum E_{VB} However, the $\Delta\mu_i$ obey some thermodynamic restrictions given by the Gibbs free energy of formation of the compound material ΔG^f so that the chemical potentials can be varied only within a range given by

$$\begin{aligned}\Delta G^f &= 2(\mu_{\mathrm{In}}^{\mathrm{In}}-\mu_{\mathrm{In}}^{\mathrm{In_2O_3}})+3(\mu_{\mathrm{O}}^{\mathrm{O_2}}-\mu_{\mathrm{O}}^{\mathrm{In_2O_3}})\\ &= 2\Delta\mu_{\mathrm{In}}+3\Delta\mu_{\mathrm{O}}. \qquad (2)\end{aligned}$$

Hence, limiting cases are

$$\Delta\mu_{\mathrm{O}}=0, \Delta\mu_{\mathrm{In}}=1/2(\Delta G_f-3\Delta\mu_{\mathrm{O}})=\Delta G_f/2, \qquad (3)$$

in the indium-rich case and

$$\Delta\mu_{\mathrm{In}}=0, \Delta\mu_{\mathrm{O}}=1/3(\Delta G_f-2\Delta\mu_{\mathrm{In}})=\Delta G_f/3, \qquad (4)$$

for the oxygen-rich case. The electron chemical potential is given by the Fermi energy E_f. As DFT is a 0K method, only total cohesive energies instead of Gibbs free energies can be directly obtained and all entropy as well as pressure dependent terms are neglected.

III. RESULTS AND DISCUSSION

A. Thermodynamics

The Fermi level dependence of the formation energy is shown in Fig. 2. The values were obtained by equation 1 for the two limiting conditions (oxygen- and indium-rich). In this diagram effects of finite cell size were already accounted for and the corrections were applied except for the band gap error. Finite size corrected defect formation energies are given in the appendix, beside uncorrected values for the indium rich and oxygen rich limit. From this picture the major defect types dominating the defect chemistry of In_2O_3 can be identified. In the indium rich regime (reducing conditions) oxygen vacancies are the donor defects with the lowest formation energy. This defect heavily confines the Fermi level to the upper part of the calculated band gap and also shows very shallow transition energies $\epsilon(0/+1)$ and $\epsilon(+1/+2)$ at the CBM. Further, the indium interstitials as well as oxygen anti sites also provide transitions within the conduction band but have high formation energies. For reduced In_2O_3 acceptor defects like the oxygen interstitial and indium vacancy attain high formation energies so that charge carriers in the conduction band remain uncompensated. In the oxygen rich regime (oxidizing conditions) mostly neutral oxygen interstitials are present. Over the whole range of the calculated band gap these defects have the lowest formation energies. The Fermi level is not restricted within the calculated band gap, but degenerate doping cannot be achieved at high oxygen pressures, because electron killer defects cross the zero energy line slightly beyond the CBM.

B. Geometry and electronic structure

The DFT results suggest that the pure material exhibits a rather anti-frenkel type disorder. Oxygen defects have generally lower formation energies as compared with indium defects.

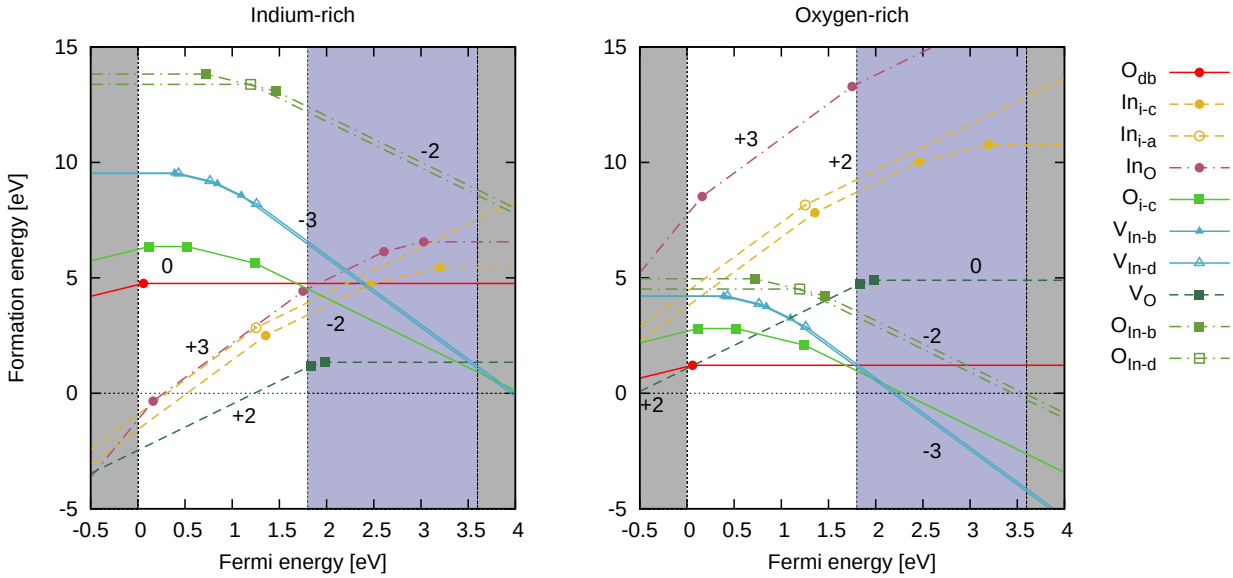

FIG. 2: Dependence of formation energy with Fermi level for the finite cell size corrected values in the two limiting cases indium rich and oxygen rich. Donor defects are represented by solid lines whereas acceptor defects and anti sites are denoted by dashed lines. The unshaded area represents the calculated band gap whereas calculated and experimental bands are indicated by different levels of shading. The VBM is located at $E_f = 0$.

1. *Donor defects*

The intrinsic donor defects of In_2O_3 have great importance for the material since these defects render the material to a good *n*-type conductor even without extrinsic doping. In the previous section the oxygen vacancy was found to have low formation energy showing transitions to lower charge states right at the calculated CBM indicating a shallow donor defect. In comparison, the indium interstitial has higher formation energies but also transitions $\epsilon(+3/+2)$ at the conduction band minimum (CBM) and transitions to even lower charge states within the conduction band resulting in instantaneous ionization of the interstitials. The *c*-site is by 0.5 eV more favorable compared with the *a*-site. Introducing an indium interstitial results in extensive outward relaxation in the first (oxygen) and second (indium) neighbor shell. Both oxygen (10% of original distance) and indium neighbors (13% *d*-site and 26% for the *b*-site In along $\langle 111 \rangle$) relax outward. Also ions at even higher distances are significantly affected by the relaxation around the interstitial. The large elastic strain can therefore be identified as the reason for the high formation energies. In contrary, the geometry hardly changes for a neutral oxygen vacancy (-2.5% -1.7% of original distance for cations and anions, respectively). Due to the the non-symmetric oxygen site, the relaxation is not complely symmetric and results in a slight displacement of the geometric center of the vacancy.

For increasing charge states the two defects show significant charge dependent relaxation which is of opposite sign for oxygen and indium neighbors. Anions are pulled inward (up to 8% for $V_O^{\cdot\cdot}$ and 16% for $In_{i-c}^{\cdot\cdot\cdot}$) while cations are pushed outwards (up to 10% for $V_O^{\cdot\cdot}$ and 2.5% $In_{i-c}^{\cdot\cdot\cdot}$). For both defects the relaxation also affects farther neighbor shells. For both donor defects the relaxations occur gradually with increasing charge state and there is no evidence for rebonding in any charge state and charge dependent relaxation can be mainly seen as the result of an ionic screening. This is in contrast to the conclusions of Lany[14,41]

Comparing the electronic structures of the two defects (Fig. 3) the simmilarity of the two donor defects is apparent. There is a remarkable change in the band structure produced by the defects compared with the ideal structure.[42] Beside the band gap which is decreased due to the introduction of the defects, there is a second gap present at higher energy values also found for tin dopants[42]. This gap is produced by the hybridization of the In-5*s* states with the defect states. As the gap width is larger for the oxygen vacancy (1.47 eV compared with 1.03 eV for the interstitial) the state has stronger resonance with the CBM. Therefore the oxygen vacancy state is assumed to be close to the conduction band edge eigentstates whereas the indium interstitial produces states above the CBM. It is also instructive to compare the band structures from the defect calculations with the band structure of In_2O_3 with a substitutional tin dopant[42], as the differences can only be seen in a slight variation of the hybridization gap width. These findings are consistent with the formation energies, as it was shown (see Fig. 2) that both defects are more stable if they are ionized. As the band gap is underestimated by DFT and there is no concesous about the actual band gap we will not include band gap corrections but note that according to Persson *et al.*[33] the transition states would not be altered with respect to the CB edge for the case of a rigid band edge correction. We further note that the changes in conduction band structures are severe

(Fig. 3), which seems to be a peculiarity of the bixbiyte structure. There is only one single conduction band state forming the CBM, altough the unit cell comprises of at least 40 atoms. Inserting a defect even in the largest supercell strongly alters the electronic band structure. Therefore, defect formation energies could be errorous, whereas transition states are less affected, since changes in electronic structure are simmilar for different charge states. Hence, we did not find any localized defect states for either potential donor defect. Further, there is uniform and gradual charge dependant relaxation of opposite sign for the two different ion types around both donor defects. Therefore, we conclude that both intrinsic donor defects produce shallow states and are capable of producing electrons within the conduction band. As the oxygen vacaancy posesses lower formation energy due to lower elastic strain, this defect is more likely to produce the non-stoichiometry as well as the *n*-type conductivity seen in In_2O_3.

Althogh In_2O_3 is highly ionic[34] the antisites are of interest. Especially the oxygen antisite can act as a donor defect and produce non-stoichiometry. More generally it can be thought of as an oxygen vacancy combined with indium interstitial. For this defect types indications of a high stability were already found in SnO_2 due to the multivalence of tin[43]. As indium also posseses a lower oxidation number which manifests in the more oxygen deficient compound In_2O, a simmilar behavior can be expected. Energetically the oxygen anti-site is very close to the interstitial, having also similar transition energies. The relaxation behavior of the defect is however, is different. In the case of the oxygen anti-site, the relaxation process is highly non-symmetric. The energy minimum for this defect configuration is found far off the regular oxygen site resulting in an indium interstitial-oxygen vacancy defect pair. Surprisingly, the minimum energy is not found at a regular interstitial *c*-site. The surplus indium atom moves within the $\{111\}$ plane and aligns with the two-fold axis. If one compares formation energies of indium interstitials and oxygen vacancies with the oxygen anti-sites, it is evident that there is no association energy for neutral defect pairs, as the sum of the formation energies equals that of the anti-site (V_O Ini defect complex). The charge state $q = 3$ is predominant for the anti-site and can be thought of as a neutral vacancy with a triply charged interstitial. This is indicated by the transition states which coincide with that of indium interstitials. As the formation energy for the anti-site is lower by 0.5 eV for this combination compared with the separated defects, there is a tendency for association. Because there were indications for association, defect calculations were also performed on defect complexes involving the regular interstitial sites. Surprisingly, all regular configurations yield higher formation energies compared with the anti-sites and were therefore not included in Fig. 2. Altough indium interstitials and oxygen anti-sites have rather high formation energies it has to be noted that the deposition of In_2O_3 are highly non equilibrium processes Therefore, interstitials and anti-sites could also contribute to the *n*-type conductivity of the material. Especially for the anti-site a low mobility can be expected so that initially produced defects could have no possibility to leave the sample even at annealing temperatures.

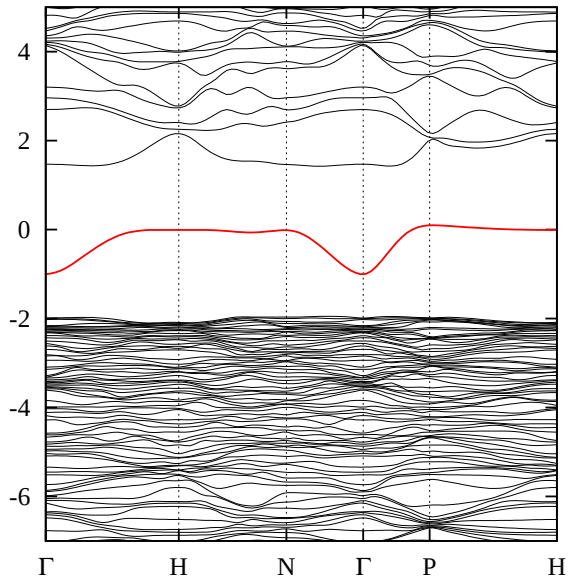

(a)oxygen vacancy

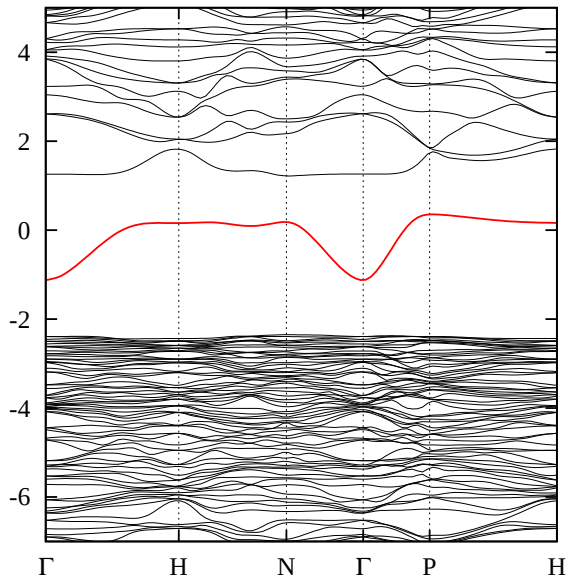

(b)indium interstitial

FIG. 3: Electronic band structures of neutral oxygen vacancy (a) and indium interstitial (b). Both defects cause a hybridization gap due to the overlap of defect states with conduction states

2. *Acceptor-like defects*

In many structures oxygen has a formal oxidation number of -2 which is an approximated value. Such a formal oxidation number can be obtained by evaluating the charge within the Bader volume of the atoms for the ideal cell. In In_2O_3 7.2 and 11.1 electrons for oxygen and indium ions respectively were

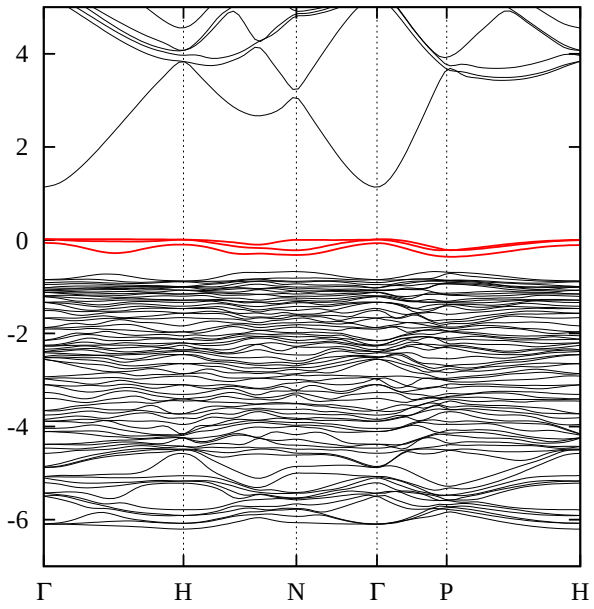

(a)oxygen Interstitial

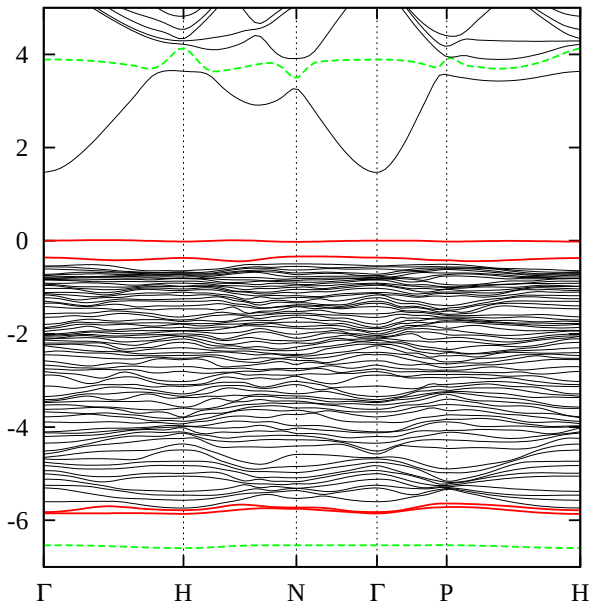

(b)oxygen dumbell

FIG. 4: Electronic band structures of oxygen interstitial defects. Both defects produce valence band related gap states. For the dumbell interstitial the states are extremely localized and resemble the molecular orbitals of doubly negtive charged peroxo-ions (O_2^{2-})

obtained. This value should be compared with the number of valence electrons per atom (6 for O and 13 for In) in the calculation. The significant amount of charge transfer indicates the ionicity of the system. For the case of the oxygen interstitials on the symmetric *c*/*a*-sites in the charge state $q = -2$, the surplus oxygen encloses a net charge which is equivalent to the charge within the Bader volume of a reference oxygen in the ideal cell, meaning that the interstitial has an oxidization state simmilar to oxygen on regular lattice sites in In_2O_3. Hence the major part of the surplus electrons is localized on the interstitial. For less negative charge states electrons are significantly removed not only from the interstitial but also from first and second neighbors. The introduction of a neutral oxygen leads to some outward relaxation (8 %). The relaxation is mainly occurs within the second neighbor oxygen shell, while displacements on nearest neighbor indium atoms are smaller than 1%. This configuration remains unchanged for more positive charge states. For negative charge states indium atoms move towards the interstitial site (8%) and oxygen neighbors are pushed farther outwards by 5% As the oxygen is highly electronegative, electrons easily get localized on it. Therefore high electron localization induces stronger relaxations for negative charge states. On the other hand for neutral, and positively charged interstitials charge is drawn of significantly from neighboring atoms resulting in a delocalized defficient charge, which gives less ionic relaxation. Additionally, constrained by symmetry, the *c*-site interstitial moves along the [111] axis towards the *a*-site (**??**) for increasingly negative charge states whereas it is only located at the geometric center for the charge state $q = 2$.

There is an alternative way of accomodating electron defficiency for oxygen interstitial defecs. In the oxygen rich regime oxygen interstitials can be present in dumb-bell configurations. The compensation of defficient charge here has a different nature and is shown to be energetically more favorable in In_2O_3, as it is the most predominant defect in the oxygen rich regime.

The charge deficiency is exclusively distributed onto two atoms giving rise to a rather localized deficient charge, whereas other atoms in the structure remain mainly unaffected. There is a slight imbalance in the amount of charge which is enclosed within the Bader volume of the participating atoms, and can be accounted to the non-symmetric position of the dumb-bell within the structure. For different configurations the “missing” deficient charge was found within the Bader volume of an oxygen in the second neighbor shell of the dimer. The excess charge on the dimer can be approximated by the sum of the total charge within the Bader volums of the dimer atoms minus the amount of electrons nominally brought in by an oxygen atom within the calculation. This yields a net Bader charge of 7.3 electrons for the *e*-site dimer compared with 7.2 in the ideal structure, indicating a doubly negative charged peroxo-ion configuration. The reaction of the dimer on removal of electrons is a shorter bond length in order to compensate for the loss of electron density. The bond length changes from 1.37 Å for the charge state $q = +2$ to 1.51Å for $q = -1$ Additionally, the dimer tends to move towards a third oxygen atom showing a slight lack of charge. Beside the dimer atoms the lattice relaxations are rather small. Therefore, there are various ways to accomodate an oxygen dumbell within the host lattice. The orientations of the different dumbell defects with respect to the threefold symmetry axis are shown in Fig. 6. The corresponding formation energies and transition levels are shown in Fig. 5. There are two

low energy configurations $O_{i-db}$and $O_{i-db,rot2}$, and another three having lower formation energies than regular *c*-site interstitials. The orientation of the most stable dumbell within a 100 plane is shown in Fig. 5. It is aligned (as much as possible) with two neighboring interstitial *c*-sites. Further, the high electron concentration between the participating atoms indicates a covalent bond inbetween (see Fig. 5).

In the electronic band structure three atomic orbital like oxygen acceptor defect bands can be found within the band gap with a strong *p*-character compared with two highly localized defect states for the dumbbell configuration (Fig. III B 2). In the first case the states resemble the the three atomic states of an isolated oxygen ion whereas in the second case the discrete energy levels of a peroxo molecule can be identified.

Further, due to symmetry, the defect states are not degenerate. The uppermost occupied defect bands can be identified as the anti-bonding π^*_{p-p} molecular orbital. The remaining oxygen dimer molecular orbitals are also highlited in the figure. For this defect, adding electrons would result in the occupancy of the conduction band since the σ^*_{p-p} can be found only 2.2 eV above the CBM, so that no ambipolar behavior can be established for this defect type. Therefore the charge state $q = -1$ denotes only a very shallow energy minimum on the total energy surface for the oxygen dumb-bell giving a transition level $\epsilon(0/-1)$ far beyond the CBM. The stability of this defect due to the fact that the binding σ_{p-p} state is located about one 1 eV below the valence band minimum.

3. Relative stability of oxygen interstitials

We also investigated the relative stability of the interchange between different interstitial configurations. In order to determine the transition state energy, we use the NEB-CI method[24–26] barrier energies were found to be below 0.3 eV for interchanges between the different covalent structures. For neutral charge states the symmetric interstitial defect configurations were found to have barriers significantly lower than 0.1 eV for transition into oxygen dumbells. It shows that these positions are no stable local minima at finite temperatures resulting in instantaneous transition into dumb-bells. Surprisingly the highly symmetric interstitial *a*-site (not included in Fig. 2) is not a stable interstitial configuration for oxygen of any charge state whereas it is stable for indium interstitials ($E_B = 0.9$eV). In summary the $O^{\times}_{i-c}$ defect is the only stable interstitial defect configuration at high Fermi energy, whereas the $O^{\times}_{i-db}$ will be the the stable covalent structure at lower Fermi energy, although transformations into other covalent structures can occur. In particular the different dumbell geometries denote low energy transition pathes for atomic movement. The orientation of the most stable dimer is a close to $\langle 110 \rangle$ direction within a (001) plane according to cubic coordinates shown in Fig.5.

4. Indium vacancies

Compared with oxygen interstitials, the indium vacancies play a minor role as an acceptor or electron killer defect. Except for very high Fermi energy, the formation energies are higher as compared with oxygen interstitial. For highly extrinsically doped In_2O_3 (ITO) a transition could occur from a donor compensation by oxygen interstitials to indium vacancies. This is possible since the favored charge states for indium ($q = -3$) vacancies and oxygen interstitials ($q = -2$) are different at high Fermi energy. The indium vacancy possesses transition levels to lower charge states throughout the band gap but the formation energies attain high values for these Fermi levels. Energetically the difference between V^{III}_{In-d} andV^{III}_{In-b}defects is less than 0.1 eV for all charge states. For both configurations a strong outward relaxation (13%) of the six neighboring oxygen can be found with a strong localization of surplus charge on the neighboring oxygen atoms. The relaxation is independent of the charge state and only found within the first neighbor shell. Compared with oxygen interstitials, defect states can observed only within the valence band. Different compensating defect types have been already discussed in literature,[7,44–46] but the differences have been accounted to interstitials in different defect complexes with tin. As the tin concentrations may become extremly high ($10^2 2cm^{-3}$)[7] for the material further defect interactions had to be accounted for in order to elucidate the relevance of indium vacancies for charge compensation. However, as indium defects are likly to have lower mobilities compared with oxygen atoms, indium vacancies could be an explanation for the non-reducible compensating defects[7,46].

IV. SUMMARY AND CONCLUSION

Within the PW-PP formalism of DFT we conducted an extensive study on the thermodynamics of various possible defect types in In_2O_3. By using different cell sizes for defect calculation, effects of finite cell size were accounted for. We found oxygen defects to dominate the defect chemistry of In_2O_3. For low Fermi energy and oxygen rich conditions oxygen interstitials in dumb-bell like geometries, equivalent to doubly negative peroxo ions were found to be the major defect where defficient charge can be efficiently compensated by a covalent oxygen bond. At higher Fermi energy, a transition to doubly negative oxygen interstitials on symmetric *c*-sites occurs whereas all other oxygen geometries become unstable. Especially for tin-doped samples, the symmetric oxygen interstitial is of great importance as it compensates the positively charged donors for high dopant concentrations. Remarkably, the difference in formation energy of oxygen interstitials and indium vacancies as a competing electron killer defect is low especially for high Fermi energies. Due to the higher charge state of the vacancy a transition can occur to compensation by indium vacancies.

In the case of donor defects we showed that the oxygen vacancy as well as the indium interstitial are both capable of producing electrons within the conduction band because posi-

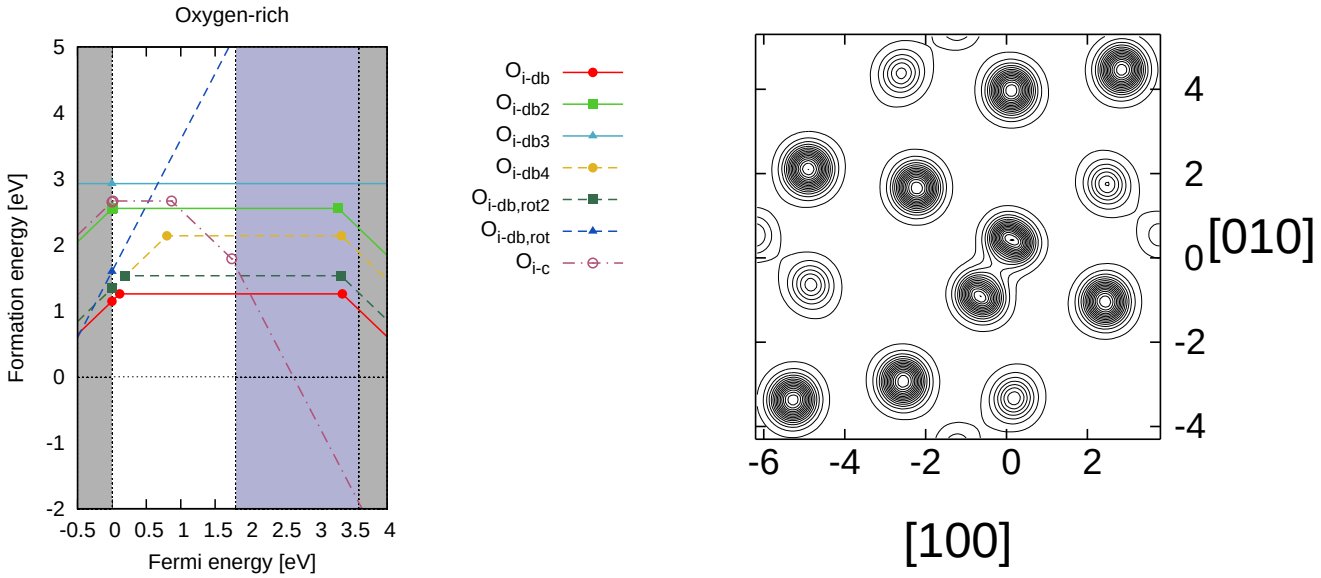

FIG. 5: Dependence of formation energy with Fermi level for the oxygen interstitials in the oxygen rich limit. A crossection of the charge density within a (001) oxygen layer shows the dimer orientation in its lowest energy configuration. The accumulation of charge between the atoms indicates the covalent bonding in between.

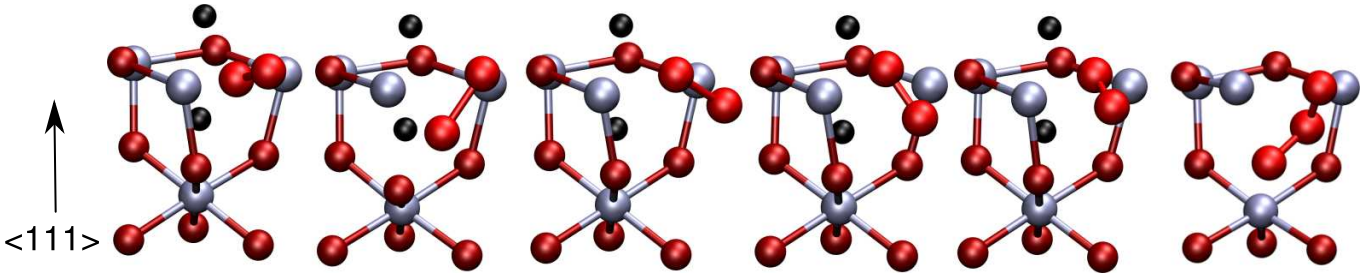

FIG. 6: Oxygen dumbell interstitial defects. The defects are located on the non-symmetric oxygen *e*-site. The dimer axis can be oriented in several directions. The most stable configuration (O_{i-db}) is shown on the very left. The two following configurations $O_{i-db2}$and $O_{i-db3}$are in linear alignment with two neighboring oxygen atoms and have longer and weaker covalent bonds. Configurations 4 ($O_{i-db,rot}$) 5 ($O_{i-db,rot2}$) denote rotated versions of O_{i-db} and are significantly lower in formation energy compared with the symmetric interstitial. For charge state $q = +2$, the dumbell defects may transform into the state as it is shown on the right. This defect posesses two equal covalent bonds as found in ozon molecules.

tively charged states are favorable within the whole band gap. Further, we identify conduction band related defect states for both defects, in agreement with the transition states.In comparison, the oxygen vacancy is more likely to produce the *n*-type behavior than the indium interstitials due to lower formation energies. Further, we showed that for the intrinsic donor defects, there may exist stable defect compexes in the form of a distorted oxygen anti-site.

V. ACKNOWLEDGMENTS

We acknowledge the financial support through the Sonderforschungsbereich 595 “Fatigue of functional materials” of the Deutsche Forschungsgemeinschaft.

[1] I. Hamberg and C. G. Granqvist, J. Appl. Phys. **60**, R123 (1986).
[2] H. L. Hartnagel, A. K. J. Dawar, and C. Jagadish, *Semiconducting Transparent Thin Films* (Institute of Physics Publishing, Bristol, 1995).
[3] L. S. Hung and C. H. Chen, Mater. Sci. Eng. R **39**, 143 (2002).
[4] C. J. Brabec, N. S. Sariciftci, and J. C. Hummelen, Adv. Funct. Mat. **11**, 15 (2001).
[5] P. Peumans, A. Yakimov, and S. R. Forrest, J. Appl. Phys. **93**, 3693 (2003).
[6] D. S. Ginley and C. Bright, MRS Bull. **25**, (2000).
[7] G. Frank and G. Köstlin, Appl Phys. A **27**, 197 (1982).
[8] V. Golovanov, M. A. Mäki-Jaskari, T. T. Rantala, G. Korotcenkov, V. Brinzari, A. Cornet, and J. Morante, Sensors and Actuators B **106**, 563 (2005).
[9] J. H. W. de Wit, J. Solid State Chem. **38**, 819 (1977).
[10] J. C. Scott, J. H. Kaufman, P. J. Brock, R. DiPietro, J. Salem, and J. Goitia, J. Appl. Phys. **79**, 2745 (1996).
[11] I. Tanaka, M. Tatsumi, M. Nkano, and H. Adachi, J. Am. Ceram. Soc. **85**, 68 (2002).
[12] I. Tanaka, F. Oba, K. Tatsumi, M. Kunisu, M. Nkano, and H. Adachi, Materials Transactions **7**, 1426 (2002).
[13] K. Y. T. Tomita and Y. Hayafuji, App. Phys. Lett **87**, 051911 (2005).
[14] S. Lany and A. Zunger, Phys. Rev. Lett. **98**, 045501 (2007).
[15] P. Erhart, A. Klein, and K. Albe, Phys. Rev. B **72**, 085213 (2005).
[16] G. Kresse and J. Furthmüller, Phys. Rev. B **54**, 11169 (1996).
[17] G. Kresse and J. Furthmüller, Comp. Mater. Sci. **6**, 15 (1996).
[18] P. E. Blöchl, Phys. Rev. B **50**, 17953 (1994).
[19] G. Kresse and D. Joubert, Phys. Rev. B **59**, 1758 (1999).
[20] J. P. Perdew, K. Burke, and M. Ernzerhof, Phys. Rev. Lett. **77**, 3865 (1996), erratum: *ibid.* **78**, 1396 (1997).
[21] P. Erhart, K. Albe, and A. Klein, Phys. Rev. B **73**, 205203 (2006).
[22] G. Makov and M. C. Payne, Phys. Rev. B **51**, 4014 (1995).
[23] R. F. W. Bader, *Atoms in Molecules – A Quantum Theory* (Oxford University Press, Oxford, 1990).
[24] G. Henkelman, G. Jóhannesson, and H. Jónsson, in *Methods for finding saddlepoints and minimum energy paths* in *Progress on theoretical chemistry and physics*, p. 269, edited by S. D. Schwartz (Kluwer Academic, Dordrecht, 2000).
[25] G. Henkelman and H. Jónsson, J. Chem. Phys. **113**, 9978 (2000).
[26] G. Henkelman, B. P. Uberuaga, and H. Jónsson, J. Chem. Phys. **113**, 9901 (2000).
[27] L. J. Sham and M. Schlüter, Phys. Rev. Lett. **51**, 1888 (1983).
[28] L. J. Sham and M. Schlüter, Phys. Rev. B **32**, 3883 (1985).
[29] P. Erhart, A. Klein, R. G. Egdell, and K. Albe, Phys. Rev. B **75**, 153205 (2007).
[30] R. L. Weiher and R. P. Ley, J. Appl. Phys. **37**, 299 (1966).
[31] A. Klein, Appl. Phys. Lett. **77**, 2009 (2000).
[32] Y. Gassenbauer, R. Schafranek, A. Klein, S. Zafeiratos, M. Hävecker, A. Knop-Gericke, and R. Schlögl, Phys. Rev. B **73**, 245312 (2006).
[33] C. Persson, Y.-J. Zhao, S. Lany, and A. Zunger, Phys. Rev. B **72**, 035211 (2005).
[34] T. L. Barr and Y. L. Liu, J. Phys. Chem. Solids **50**, 657 (1989).
[35] A. Klein (unpublished).
[36] V. I. Anisimov, J. Zaanen, and O. K. Andersen, Phys. Rev. B **44**, 943 (1991).
[37] A. I. Liechtenstein, V. I. Anisimov, and J. Zaanen, Phys. Rev. B **52**, R5467 (1995).
[38] S. L. Dudarev, G. A. Botton, S. Y. Savrasov, C. J. Humphreys, and A. P. Sutton, Phys. Rev. B **57**, 1505 (1998).
[39] M. Marezio, Acta Cryst **20**, 723 (1966).
[40] D. R. Lide, *Handbook of Chemistry and Physics* (CRC Press, ADDRESS, 2005).
[41] S. Lany and A. Zunger, Phys. Rev. B **72**, 035215 (2005).
[42] O. N. Mryasov and A. J. Freeman, Phys. Rev. B **64**, 233111 (2001).
[43] C. Kilic and A. Zunger, Phys. Rev. Lett. **88**, 095501 (2002).
[44] O. Warschkow, D. E. Ellis, G. B. González, and T. O. Mason, J. Am. Ceram. Soc. **86**, 1700 (2003).
[45] O. Warschkow, D. E. Ellis, G. B. González, and T. O. Mason, J. Am. Ceram. Soc. **86**, 1707 (2003).
[46] O. Warschkow, L. Miljacic, D. E. Ellis, G. B. González, and T. O. Mason, J. Amer. Ceramic Soc. **89**, 616 (2006).

Defect	charge	H_f^{O} [eV]	H_f^{In} [eV]	H_f^{O} [eV]	H_f^{In} [eV]	Δ
$\mathrm{O_{i-db}}$	0	4.76	1.21	4.80	1.26	-0.04
	+1	4.71	1.16	4.40	0.85	0.31
$\mathrm{In_{i-c}^{\cdots}}$	0	4.59	9.91	6.31	11.63	-1.72
	+1	2.13	7.45	2.07	7.39	0.06
	+2	0.11	5.43	-1.70	3.62	1.81
	+3	-1.57	3.76	-4.73	0.59	3.16
$\mathrm{In_{i-a}^{\cdots}}$	+2	0.50	5.82	-1.01	4.31	1.51
	+3	-0.92	4.40	-4.09	1.23	3.17
$\mathrm{In_O}$	0	6.15	15.02	6.97	15.84	-0.82
	+1	3.35	12.22	3.41	12.28	-0.06
	+2	1.13	10.00	-0.27	8.60	1.40
	+3	-0.64	8.23	-3.67	5.20	3.03
	+4	-0.16	8.71	-5.05	3.82	4.89
	+5	-3.00	5.87	-6.65	2.22	3.65
$\mathrm{O_{i-c}^{\prime\prime}}$	-2	8.12	4.57	7.65	4.10	0.47
	-1	6.87	3.33	6.79	3.24	0.09
	0	6.35	2.81	6.21	2.67	0.14
	1	6.27	2.72	5.90	2.36	0.36
	2	6.75	3.20	5.79	2.24	0.96
$\mathrm{O_{i-a}^{\prime\prime}}$	-2	8.92	5.37	8.87	5.32	0.05
	-1	7.68	4.13	7.82	4.28	-0.14
	0	6.82	3.27	7.08	3.54	-0.27
$\mathrm{V_{In-b}^{\prime\prime\prime}}$	0	9.58	4.25	9.49	4.17	0.09
	-1	9.89	4.56	8.86	3.54	1.02
	-2	10.68	5.35	8.35	3.03	2.33
	-3	12.06	6.73	7.97	2.64	4.09
$\mathrm{V_{In-d}^{\prime\prime\prime}}$	0	9.45	4.13	9.38	4.06	0.07
	-1	9.82	4.50	8.79	3.47	1.04
	-2	10.71	5.38	8.36	3.04	2.34
	-3	12.18	6.86	8.15	2.83	4.03
$\mathrm{V_O}$	0	1.34	4.89	1.44	4.99	-0.10
	+1	-0.67	2.88	-0.75	2.80	0.09
	+2	-2.33	1.22	-2.94	0.61	0.61
$\mathrm{O_{i-db}}$	-1			7.86	4.31	
	+ 2			4.20	0.65	
$\mathrm{O_{i-db2}}$	-1			9.09	5.54	
	0			6.09	2.55	
	+1			5.79	2.25	
	+2			5.68	2.13	
	0			6.47	2.92	
	+2			6.17	2.62	
$\mathrm{O_{i-db,rot}}$	-1			8.72	5.18	
	0			5.68	2.13	
	+1			4.59	1.04	
	+2			4.38	0.83	
$\mathrm{O_{i-db,rot2}}$	-1			8.11	4.56	
	0			5.07	1.53	
	+1			4.59	1.04	
	+2			4.38	0.83	
$\mathrm{O_{i-db3}}$	+2			3.96	0.42	
	+3			3.80	0.25	
$\mathrm{O_{In-b/d}}$	-2			14.83	5.97	
	-1			14.25	5.38	
	0			13.82	4.95	

TABLE II: Formation energies for finite cell size corrected defects and corrections for the dilute limit.